Nano Research
2021, 14(7): 2277–2284

ISSN 1998-0124 CN 11-5974/O4
https://doi.org/10.1007/s12274-020-3222-x

Research Article

Engineering electrochemical actuators with large bending strain based on 3D-structure titanium carbide MXene composites

Tong Wang[1,2], Tianjiao Wang[1,2], Chuanxin Weng[1], Luqi Liu[1], Jun Zhao[1,2] (✉), and Zhong Zhang[1,2] (✉)

[1] *CAS Key Laboratory of Nanosystem and Hierarchical Fabrication, CAS Center for Excellence in Nanoscience, National Center for Nanoscience and Technology, Beijing 100190, China*
[2] *University of Chinese Academy of Science, Beijing 100049, China*

Received: 6 August 2020 / **Revised:** 9 October 2020 / **Accepted:** 3 November 2020

ABSTRACT

Electrically responsive electrochemical actuators that contain a polymer electrolyte membrane laminated between two electrodes have attracted great attention due to their potential applications in smart electronics, wearable devices, and soft robotics. However, some challenges such as the achievement of large bending strain under low applied voltage and fast ion diffusion and accumulation still exist to be resolved. The key to the solution lies in the choice of electrode materials and the design of electrode structures. In this study, an engineering electrochemical actuator that presents large bending strain under low applied voltage based on MXene/polystyrene-MXene hybrid electrodes is developed. The developed electrochemical actuator based on the MXene/polystyrene-MXene 3D-structure is found to exhibit large bending strain (ca. 1.18%), broad frequency bandwidth, good durability (90% retention after 10,000 cycles) and considerable Young's modulus (ca. 246 MPa). The high-performance actuation mainly stems from the excellent properties of MXene and 3D-structure of the electrode. The MXene provides excellent mechanical strength and high electrical conductivity which facilitate strong interaction and rapid electron transfer in electrodes. The 3D architectures formed by polystyrene microspheres generate unimpeded ion pathways for ionic short diffusion and fast injection. This study reveals that the 3D-structure hybrid electrodes play a crucial role in promoting the performance of such electrochemical actuators.

KEYWORDS

electrochemistry, actuators, MXene, composite materials

1 Introduction

Among soft actuators stimulated by electricity [1, 2], magnetism [3, 4], light [5–7], temperature [8–10] and so on, electroactive polymer (EAP) actuators have great advantages due to their activated and controllable actuation performance under different frequencies and voltages. To date, EAP actuators have received enormous interest as artificial muscles for applications in smart electronics, wearable devices, and soft robotics due to their light weight, high flexibility, and simple fabrication process [11]. As one of the most attractive EAP actuators, electrochemical actuators are composed of an ionic exchangeable polymer membrane as the electrolyte and two conducting electrodes covering the two opposite faces of the electrolyte. Under electrical stimulation, cations and anions migrate to the cathodes and anodes respectively and electrical energy is stored in a double interface. The different molecular sizes of cations and anions lead to volumetric shrinkage and expansion of the electrodes, which will generate the bending strain of electrochemical actuators and convert electrical energy to mechanical energy.

The bending strains are caused not only by ion transfer between electrodes and the electrolyte, but also by ion insertion directly into electrodes. Therefore, the material and structure of electrodes play vital roles in the preparation of high-performance electrochemical actuators. Traditionally, the utilized electrode materials are noble metals such as gold, platinum, and silver. Although they have good electrical conductivity, there are some serious drawbacks, such as the cracks in the electrodes after multiple bending that result in poor durability, the high cost of noble metals, and the time-consuming process [12]. Recently, carbon materials and its composites have been employed as electrodes due to their excellent electrical conductivity, high capacitance, and good structural stability [13]. And the developed electrochemical actuators with carbon materials and its composites exhibit excellent electrical, electrochemical and actuation properties such as considerable bending strain, fast response speed, and high cycling durability. According to the categories of electrode materials, there are four kinds of electrochemical actuators: carbon materials [14–17], metals or metal oxides-carbon composites [18–20], polymers-carbon composites [21–24], and heteroatoms doped carbon materials [25–28]. Up to now, most actuators reported in the literature have achieved considerable bending deformation [16–18, 24, 25]. While the sluggish transport of mobile ions and lack of intercalated ions in the electrode still exist to be resolved. Therefore, the development of electrode with excellent properties and unimpeded structure is highly needed.

MXene, a young family of two-dimensional (2D) materials, are transition metal carbides and/or nitrides with the formula $M_{n+1}X_nT_x$, where M represents early transition metals; X represents

Address correspondence to Zhong Zhang, zhong.zhang@nanoctr.cn; Jun Zhao, zhaoj@nanoctr.cn

carbon and/or nitrogen; T_x represents surface terminations; n = 1, 2, or 3 [29, 30]. They have been widely explored for catalysis [31], energy storage devices [32–35], sensors [36, 37], electromagnetic interference shielding [38–41], etc. Among different types of MXene, $Ti_3C_2T_x$ has been the most studied to date because of its metal-like conductivity, high storage capacity and fascinating mechanical property. Thus, $Ti_3C_2T_x$ is a good candidate electrode material for electrochemical actuators and $Ti_3C_2T_x$-based actuators have already been reported [42, 43].

However, because of the restacking and aggregation of $Ti_3C_2T_x$ sheets resulted from van der Waals forces and hydrogen bonds, it is difficult for ions to migrate into the electrode. So changing the stacked layered structures of $Ti_3C_2T_x$ is a challenging issue. Therefore, $Ti_3C_2T_x$ composites with various polymers, such as polyvinyl alcohol [44] and polypyrrole [45], have been developed to avoid this issue. More importantly, the method of adding polymer can change the morphology and structure of the material. 1D and 2D structures lead to relatively slow ion diffusion in the composite electrodes, eventually resulting in insufficient actuation performance. The 3D structure with multidirectional fast electron transfer can be used to provide much faster ion diffusion, which is required to generate high-performance actuation of electrochemical actuators. In a previous study, MXene and positively charged polystyrene (PS) composites were fabricated by the compression molding method following with an electrostatic assembly approach, showing outstanding electromagnetic interference shielding performance because of the high conductivity of MXene and the highly efficient conducting network at the surface of PS microspheres [46]. The efficient conducting network formed in the electrode is also important for electrochemical actuators. PS microspheres have not been used as the electrode material for electrochemical actuators. However, it can provide unimpeded ion pathways for ion short diffusion and fast injection, giving the actuator fast response and large deformation. Also, 3D architecture of MXene with PS microspheres has not yet been explored as electrodes for highly bendable electrochemical actuators.

In this work, we developed an engineering electrochemical actuator incorporating MXene and uncharged PS microspheres composites and used the vacuum-filtration method to fabricate MXene/PS-MXene 3D-structure. The MXene/PS-MXene electrode material with the bilayer structure contains the MXene layer and the MXene/PS layer. To enhance the mechanical stiffness and electrical conductivity of electrodes, the MXene/PS layer was covered by a layer of pure MXene. The MXene/PS layer provides conductive networked structures and unimpeded ion pathways for mobile ions through the 3D architecture of PS microspheres covered by $Ti_3C_2T_x$. As a result, the MXene/PS-MXene actuators exhibited superior actuation performance in comparison with MXene actuators. This MXene/PS-MXene 3D-structure exhibits efficient electron transport and fast ion diffusion, making it an ideal candidate as flexible electrode materials for electrochemical actuators. The main purpose of our study is to confirm the 3D structure playing an important role in promoting the actuation performance as well as guiding the development of next-generation electrochemical actuators.

2 Experimental

2.1 Materials

1-ethyl-3-methylimidazolium tetrafluoroborate ($EMIBF_4$), lithium fluoride (LiF) powders, poly(vinyl alcohol) (PVA) (1799 type) and PS microspheres (the diameter is 1 μm and 0.6 μm respectively) dispersion were provided by Shanghai Macklin Biochemical Co., Ltd. China. Ti_3AlC_2 powders were purchased from Jilin 11 Technology Co., Ltd. China. Poly(vinylidene fluoride) (PVDF) powders (Kynar k721) were purchased from Arkema Co., Ltd. *N,N*-dimethylformamide (DMF) and sulfuric acid (H_2SO_4) were supplied by Beijing Chemical Works Co. Ltd., China. All the materials were used as received.

2.2 Synthesis of aqueous dispersion of $Ti_3C_2T_x$

$Ti_3C_2T_x$ dispersion was synthesized by the minimally intensive layer delamination (MILD) method as reported in the literature [47]. Specifically, 3.2 g LiF powders were added into 40 mL HCl (9 M) and mechanically stirred at room temperature for 20 min to obtain a uniform transparent solution. Then 2 g Ti_3AlC_2 powders were slowly added into the solution and the etching was carried out at 35 °C for 24 h. Next, the synthesized multilayer $Ti_3C_2T_x$ was washed with deionized water and centrifuged at 3,500 rpm alternately several times to remove residual ions until the supernatant reached a pH value of 6.0. Finally, the $Ti_3C_2T_x$ in the sediment was further delaminated by manual shaking and centrifuged at 3,500 rpm alternately several times to get the aqueous dispersion of $Ti_3C_2T_x$.

2.3 Preparation of $Ti_3C_2T_x$ electrode layers

The aqueous dispersion of $Ti_3C_2T_x$ was vacuum-filtered through a cellulose membrane with an average pore size of ca. 0.22 μm. The obtained wet films were dried before they were peeled off.

2.4 Preparation of $Ti_3C_2T_x$/PS-$Ti_3C_2T_x$ electrode layers

The $Ti_3C_2T_x$ dispersion (2 mg·mL^{-1}) and uncharged PS microspheres dispersion (50 mg·mL^{-1}) were mixed together by stirring. The mass ratio of $Ti_3C_2T_x$ to PS microspheres was controlled at 1:1. The dispersion of $Ti_3C_2T_x$/PS was vacuum-filtered through a cellulose membrane with an average pore size of ca. 0.22 μm. Then the $Ti_3C_2T_x$ dispersion was vacuum-filtered continuously until the solvent was filtered out. The obtained wet films were dried up before they were peeled off.

2.5 Preparation of $EMIBF_4$/PVDF electrolyte layers

0.5 g PVDF powders were dissolved in 10 mL DMF at 70 °C and mechanically stirred for 30 min to obtain a uniform transparent solution. Then 1 g $EMIBF_4$ was added into the solution and the stirring was kept at the same temperature for 90 min. Finally, the electrolyte layers were prepared by casting the DMF solution of $EMIBF_4$/PVDF onto a glass plate and then dried at 80 °C for 2 h to remove the solvent.

2.6 Preparation of H_2SO_4/PVA electrolyte layers

1 g H_2SO_4 was added into 10 mL deionized water and mechanically stirred at room temperature for 20 min to obtain a uniform solution. Then 1 g PVA was dissolved in the solution at 85 °C to obtain a uniform transparent solution under continuous stirring. Finally, the electrolyte layers were prepared by casting the H_2SO_4/PVA solution onto a Teflon mould and then dried at 40 °C for 4 h to remove the solvent.

2.7 Assembly of the sandwiched structure actuator

The different electrolyte layers prepared above were peeled off from the mould and then laminated by two as-prepared electrode layers. Afterwards, the sandwiched structure actuators were assembled by the hot-pressing method. The $EMIBF_4$/PVDF actuators were pressed at 80 °C under 0.28 ± 0.02 MPa for 5 min and the H_2SO_4/PVA actuators were pressed at 40 °C under the

same pressure for 5 min. Finally, the assembled actuators were aged at room temperature for 24 h and then cut into strips with a size of 5 × 20 mm^2.

2.8 Sample characterizations

The morphology of samples was observed by using a scanning electron microscope (SEM, Hitachi S-4800). An X–ray diffractometer (XRD, Smartlab-9) was used to examine the phase structure of the materials. The electrical conductivity was measured by a four-probe method with a Kethley SCS-4200. The cyclic voltammetry (CV) experiments were carried out on a VMP3 electrochemical station at the scan rate of 10 mV·s^{-1} (vs. Ag/AgCl). The specific capacitance C_m is calculated using the following equation

$$C_m = \frac{\int_{V_1}^{V_2} IdV}{\Delta V v m} \quad (1)$$

where ΔV, v and m are the potential window, scan rate and weight of the electrode, respectively. The electrochemical impedance spectroscopy (EIS) measurements were carried out over a frequency range from 100 mHz to 100 kHz under a sinusoidal voltage with an amplitude of 10 mV. The galvanostatic charge-discharge (GCD) tests were carried out at the current density of 1 A·g^{-1}. A dynamic mechanical thermal analyzer (DMTA, TA Q800) was employed to evaluate the mechanical properties of the samples. The static tensile tests were conducted in strain ramp mode with a pre-force of 0.01 N and a ramp rate of 0.1%·min^{-1}.

2.9 Actuation performance tests

The electrical power was supplied by a Tektronix arbitrary function generator (AFG3011) and the bending displacements were measured using a Keyence LK-G5001 laser displacement sensor whose measuring range was ± 3 cm. The vertical distance of the recorded point was set to be 16 mm from the fixed end. The strain ε and strain rate ε_γ are calculated using the following equations

$$\varepsilon = \frac{2d\delta}{l^2 + \delta^2} \quad (2)$$

$$\varepsilon_\gamma = 4\varepsilon f \quad (3)$$

where δ, d, l, and f are the bending displacement, thickness, vertical distance of the recorded point to the fixed end of actuators and applied frequency, respectively.

3 Results and discussion

$Ti_3C_2T_x$, the most widely studied one in the MXene family, has excellent electrical conductivity, charge storage capacity, and mechanical properties. Therefore, $Ti_3C_2T_x$ and its composite materials are chosen to be used as electrodes of electrochemical actuators. Among various synthesis methods of $Ti_3C_2T_x$ dispersion, the minimally intensive layer delamination (MILD) method is used to prepare $Ti_3C_2T_x$ dispersion through *in situ* HF formation from fluoride salts [47]. It can be seen from the SEM image (Fig. S1 in the Electronic Supplementary Material (ESM)) that the size of $Ti_3C_2T_x$ flake is around 2 μm and the structure is relatively complete. Due to the van der Waals force and hydrogen bond interaction, the $Ti_3C_2T_x$ film prepared by vacuum filtration is closely re-stacked (Fig. 1(a)), where the layer spacing is ca. 1.22 nm (Fig. S2 in the ESM). In addition, the prepared $Ti_3C_2T_x$ film also has excellent electrical conductivity and high Young's modulus, which are ca. 4,690 S·cm^{-1} and ca. 13.4 GPa, respectively (Fig. S3 in the ESM). The excellent

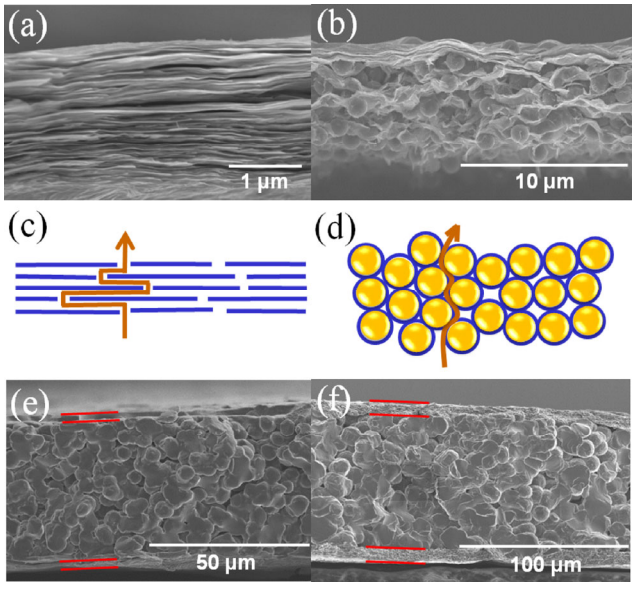

Figure 1 Morphological characterizations and schematic diagrams of electrode films and actuators. Cross-sectional SEM images of (a) the pure MXene electrode and (b) the MXene/PS-MXene electrode. Schematic diagrams of ion pathways in (c) MXene films and (d) MXene/PS layer. The blue lines and circles represent MXene sheets; the yellow spheres represent PS microspheres; the brown arrows represent ion pathways. Cross-sectional SEM images of (e) the MXene actuator and (f) the MXene/PS-MXene actuator. The overall thickness of the MXene actuator is 64 μm, in which the thickness of the MXene electrode layer is 2 μm and the thickness of the $EMIBF_4$/PVDF electrolyte layer is 60 μm. The overall thickness of the MXene/PS-MXene actuator is 95 μm, in which the thickness of the MXene/PS-MXene electrode layer is 6 μm, and the thickness of the $EMIBF_4$/PVDF electrolyte layer is 83 μm.

electrical conductivity of $Ti_3C_2T_x$ comes from the alternating atomic layer structure of Ti and C. The known strongest Ti–C bond and the hydrogen bond interaction between $Ti_3C_2T_x$ sheets both contribute to ultra-high Young's modulus. However, due to the tightly re-stacked structure of $Ti_3C_2T_x$ films, the migration of ions in $Ti_3C_2T_x$ films becomes difficult. Therefore, PS microspheres were added into $Ti_3C_2T_x$ to change the migration pathways of ions so that ions can easily diffuse and aggregate in the electrode layer (Figs. 1(c) and 1(d)). In order to enhance the mechanical properties of the MXene/PS hybrid layer and reduce the voltage drop along the surface of actuators, the MXene layer was filtered on the MXene/PS hybrid layer and the MXene/PS-MXene composite film was prepared (Fig. 1(b)). The Young's modulus of MXene/PS-MXene film, which is ca. 3.3 GPa, is an order of magnitude lower than that of MXene film (Fig. S3 in the ESM). According to Fig. S4 in the ESM, the surface of MXene films is flat without observable undulations or wrinkles. However, the surface of the MXene/PS layer has pores. The PS microspheres that are not wrapped by $Ti_3C_2T_x$ sheets are clearly visible, and the surface of the PS microspheres that are wrapped by $Ti_3C_2T_x$ sheets shows undulations and wrinkles. The surface of the MXene layer in MXene/PS-MXene films is no longer flat and has obvious wrinkles due to the presence of the MXene/PS layer.

$EMIBF_4$/PVDF films and H_2SO_4/PVA films were prepared as electrolyte layers. According to the measurements of mechanical properties (Fig. S3 in the ESM), the Young's modulus of $EMIBF_4$/PVDF films is an order of magnitude higher than that of H_2SO_4/PVA films because $EMIBF_4$/PVDF films are solid while H_2SO_4/PVA films are in a gel state. After that, three types of actuators were prepared by hot pressing method. They are MXene-$EMIBF_4$/PVDF-MXene actuators (MXene actuators or $EMIBF_4$/PVDF actuators), MXene-H_2SO_4/PVA-MXene actuators

(H_2SO_4/PVA actuators), and MXene-MXene/PS-$EMIBF_4$/PVDF-MXene/PS-MXene actuators (MXene/PS-MXene actuators). The SEM images (Figs. 1(e) and 1(f) and Fig. S5 in the ESM) exhibit the obvious sandwiched structure of actuators, which has been marked with parallel red lines. Figure S6 in the ESM shows good interlayer adhesion between the electrode layer and the intermediate electrolyte layer which should be due to the good compatibility among all components and is very important for the high cycling stability of actuators.

Figure 2 shows the performances and properties of $EMIBF_4$/PVDF actuators and H_2SO_4/PVA actuators. The Young's modulus of $EMIBF_4$/PVDF actuators is ca. 765 MPa while that of H_2SO_4/PVA actuators is ca. 40 MPa. The Young's modulus of $EMIBF_4$/PVDF actuators is an order of magnitude higher than that of H_2SO_4/PVA actuators because $EMIBF_4$/PVDF films have higher Young's modulus than H_2SO_4/PVA films. Under a 0.1 V, 0.01 Hz square wave voltage, the peak-to-peak displacement of $EMIBF_4$/PVDF actuators is ca. 2.5 times that of H_2SO_4/PVA actuators. Because the size difference between EMI^+ and BF_4^- is larger than that between H^+ and SO_4^{2-}, $EMIBF_4$/PVDF actuators can produce more significant bending deformation. In addition, it is found that $EMIBF_4$/PVDF actuators remain at the maximum displacement after reaching it, while the bending displacement of H_2SO_4/PVA actuators increases with the time of applied voltage, which is probably caused by different energy storage mechanisms. It is assumed that $EMIBF_4$/PVDF actuators take the mechanism of electric double layer capacitance (EDLC), while H_2SO_4/PVA actuators take pseudo-capacitance to store energy. To confirm this explanation, their electrochemical properties need to be checked and compared in more detail.

According to the CV measurement (Fig. 2(c)), the CV curve of $EMIBF_4$/PVDF actuators is more rectangular than that of H_2SO_4/PVA actuators. The CV curve of H_2SO_4/PVA actuators is near-rectangular rather than shows significant redox peaks because the valence of Ti in $Ti_3C_2T_x$ is continuously changing during charging and discharging, as reported in the literature [48]. From the GCD profiles of Fig. S8 in the ESM, it can also be seen that the GCD curve of $EMIBF_4$/PVDF actuators presents a more regular triangle compared to that of H_2SO_4/PVA actuators. Both CV measurement and GCD tests illustrate that $EMIBF_4$/PVDF actuators and H_2SO_4/PVA actuators take different energy storage mechanisms. Furthermore, the capacitance of the H_2SO_4/PVA actuators (ca. 87 $F{\cdot}g^{-1}$) is higher than that of the $EMIBF_4$/PVDF actuators (ca. 55 $F{\cdot}g^{-1}$). To explain this result, the EIS measurements are carried out. As shown in Fig. S7 in the ESM, R_0 in the equivalent circuit model represents the internal resistance of actuators; Q_1 and R_1 in parallel is the contact resistance between the clamped metal electrode and the actuator; Z_w is the diffusion impedance indicating the diffusion capacity of ions in the actuator; and C_1 represents the intercalation capacitance indicating the accumulation of charge. The specific values of above parameters for two actuators are listed in Table S1 in the ESM. According to the simulated analysis, the internal resistance for $EMIBF_4$/PVDF actuators is higher than that for H_2SO_4/PVA actuators. Since electrode materials used for these two actuators are exactly the same, the contact resistances of the two actuators should be close to each other. Concerning the diffusion impedance, the value for H_2SO_4/PVA actuators is lower than that for $EMIBF_4$/PVDF actuators due to the larger volume of ions in ionic liquid, which are more difficult to diffuse. The values of intercalation capacitance of two actuators are at almost the same level. Therefore, the main reason for the smaller capacitance of $EMIBF_4$/PVDF actuators is that the large ions in ionic liquid are more difficult to diffuse. However, compared with H_2SO_4/PVA actuators, $EMIBF_4$/PVDF actuators have better mechanical properties and larger bending displacement and voltage window.

Then the performances and properties of MXene actuators and MXene/PS-MXene actuators in which the diameter of PS microspheres is 1 μm are compared in Fig. 3. According to the measurements of mechanical properties, the Young's modulus of MXene actuators is higher than that of MXene/PS-MXene actuators (ca. 246 MPa). This is because the addition of PS microspheres changed the structure of electrodes and declined the mechanical properties of electrodes. Fig. 3(b) and Fig. S9 in the ESM show the actuation performance of MXene actuators and MXene/PS-MXene actuators. MXene/PS-MXene actuators have a greater bending deformation than MXene actuators. Especially, under a 1.5 V, 0.1 Hz square wave voltage, the peak-to-peak displacement and peak-to-peak strain of

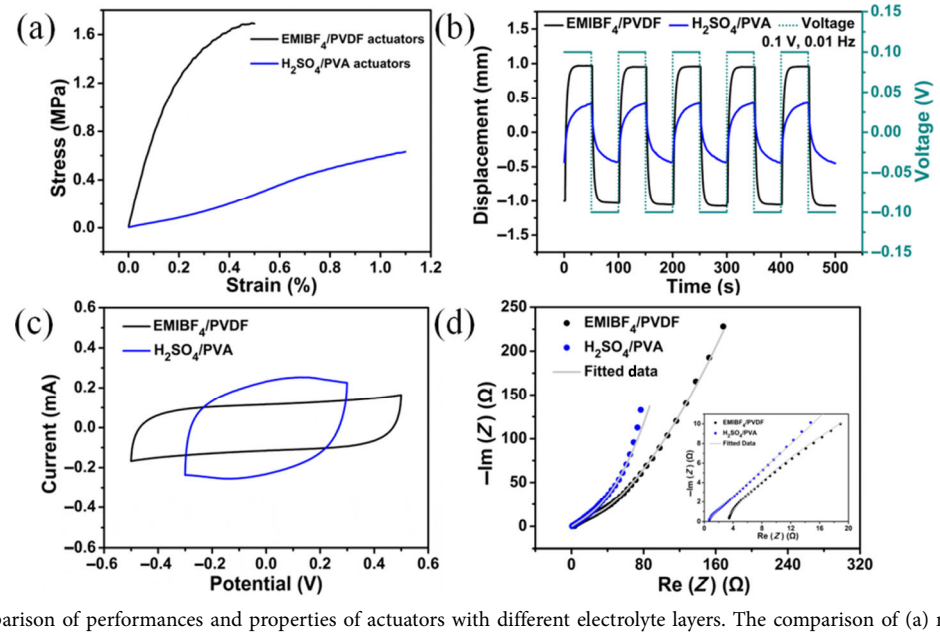

Figure 2 The comparison of performances and properties of actuators with different electrolyte layers. The comparison of (a) mechanical properties, (b) actuation performances, (c) CV experiments and (d) EIS measurements between $EMIBF_4$/PVDF actuators and H_2SO_4/PVA actuators. Inset in part (d): The EIS results in the magnified high-frequency region.

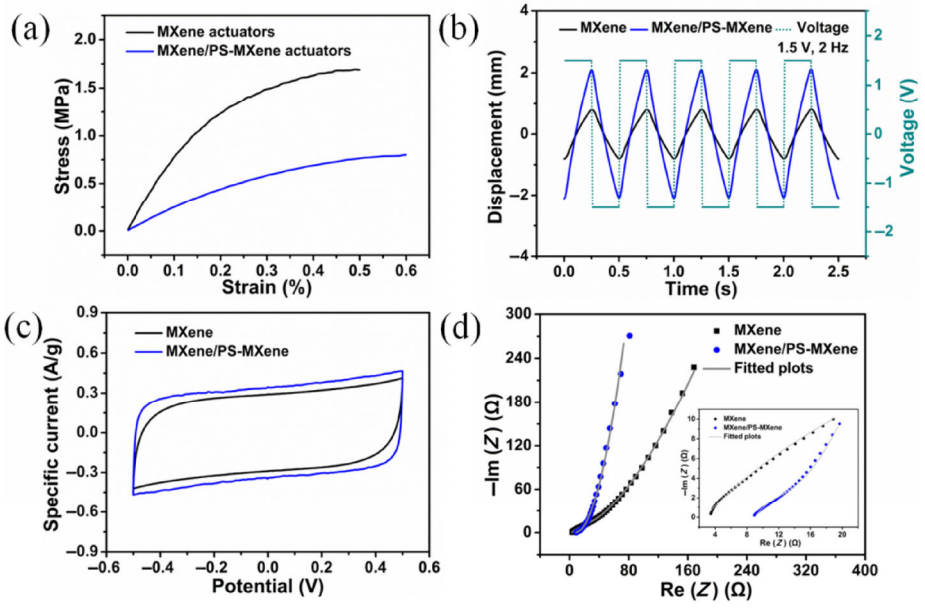

Figure 3 The comparison of performances and properties of actuators with different electrode layers. The comparison of (a) mechanical properties, (b) actuation performances, (c) CV experiments, and (d) EIS measurements between MXene/PS-MXene actuators and MXene actuators. Inset in part (d): The EIS results in the magnified high-frequency region.

MXene/PS-MXene actuators (1 μm PS microspheres) reached 35 mm and 1.18%, respectively. On the one hand, MXene/PS-MXene actuators have a lower Young's modulus; on the other hand, ions are easier to migrate and diffuse in the MXene/PS-MXene electrode. So more ions will accumulate in the electrode, resulting in the more considerable deformation of MXene/PS-MXene actuators. Furthermore, according to Fig. 3(b), MXene/PS-MXene actuators have a higher response rate (16.8 mm·s^{-1}) compared with that of MXene actuators under 1.5 V, 2 Hz square wave voltage, which is 6.44 mm·s^{-1}. The higher response rate of MXene/PS-MXene actuators is contributed to the unimpeded ion pathways established in the electrode layer.

According to CV curves of the two actuators, MXene/PS-MXene actuators have a larger capacitance than MXene actuators, indicating that changing migration pathways of ions is useful to improve electrochemical properties of the material. According to the simulated analysis of EIS measurements (Table S2 in the ESM), the internal resistance, contact resistance and intercalation capacitance of the two actuators are close to each other. However, the diffusion impedance of MXene/PS-MXene actuators is significantly smaller than that of MXene actuators, indicating that ions are more likely to diffuse in the electrode after changing the migration pathways.

Figure 4 is the actuation performance of MXene/PS-MXene actuators (1 μm PS microspheres) and MXene actuators at different frequencies and voltages. At a fixed voltage of 0.5 V, the peak-to-peak displacement decreases with increasing applied frequency because the anions and cations in the electrolyte layer will have more time to migrate and accumulate at the

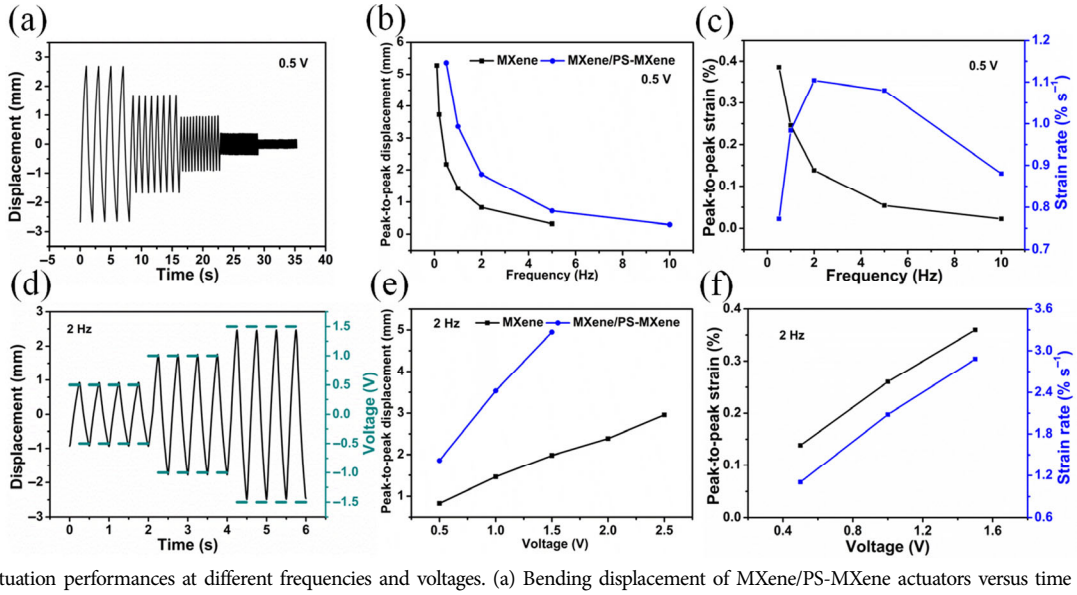

Figure 4 Actuation performances at different frequencies and voltages. (a) Bending displacement of MXene/PS-MXene actuators versus time under ± 0.5 V square wave voltage at different frequencies. (b) Peak-to-peak displacement of MXene actuators and MXene/PS-MXene actuators under ± 0.5 V square wave voltage at different frequencies. (c) Peak-to-peak strain and strain rate of MXene/PS-MXene actuators under ± 0.5 V square wave voltage at different frequencies. (d) Bending displacement of MXene/PS-MXene actuators versus time under different voltage at the frequency of 2 Hz. (e) Peak-to-peak displacement of MXene actuators and MXene/PS-MXene actuators under different voltage at the frequency of 2 Hz. (f) Peak-to-peak strain and strain rate of MXene/PS-MXene actuators under different voltage at the frequency of 2 Hz.

positive and negative electrodes of actuators at a lower frequency, thereby generating larger bending deformation. However, after the applied frequency exceeds 10 Hz, the bending displacement of actuators is very weak, which can be regarded as no actuation phenomenon. This is because the time for ions to migrate at a higher frequency is very short, making it difficult to achieve bending deformation. In addition, it was also found that the peak-to-peak displacement of MXene/PS-MXene actuators is larger than that of MXene actuators at the same frequency and the response frequency of MXene/PS-MXene actuators reaches 10 Hz which is twice that of MXene actuators (5 Hz). All these are contributed to the change of migration pathways caused by the addition of PS microspheres. In MXene/PS-MXene actuators, more ions migrate and accumulate at the electrode, resulting in greater bending displacement at the same frequency. In addition, ions can migrate faster in the MXene/PS-MXene electrode, resulting in the range of response frequency wider. In Fig. 4(c), it can be seen that the peak-to-peak strain decreases as the applied frequency increases and the trend of peak-to-peak strain is consistent with that of peak-to-peak displacement. However, the strain rate reaches a maximum at 2 Hz. When the frequency is lower than 2 Hz, the strain rate speeds up with increasing frequency, indicating that the bending speed of actuators is faster near the equilibrium position and gradually becomes slower as the degree of curvature increases, which is consistent with the actual phenomenon. When the frequency is higher than 2 Hz, the positive and negative poles of applied voltage switch so fast that the migration rate of ions may not keep up with the change of voltage, making the strain rate decreases.

At a fixed frequency of 2 Hz, the peak-to-peak displacement increases with increasing applied voltage because the electric field strength between the two electrodes of actuators increases at high voltage, causing more anions and cations to migrate and accumulate at the positive and negative electrodes and making the bending deformation more significant. In addition, it can also be found that the peak-to-peak displacement of MXene/PS-MXene actuators is larger than that of MXene actuators at the same voltage because the change of ion pathways in the MXene/PS-MXene electrode reduces the migration resistance of ions and makes ions migrate faster, resulting in larger bending displacement at the same voltage. Figure 4(f) shows that both the peak-to-peak strain and strain rate increase with increasing applied voltage because the strong electric field strength between the two electrodes at high voltage accelerates the migration of ions, thus causing the strain rate of actuators increasing. Figs. S10 and S11 in the ESM show the details of actuation performances with MXene actuators and MXene/PS-MXene actuators where the size of PS microspheres is 0.6 μm. Compared with MXene actuators, both MXene/PS-MXene actuators with different sizes of PS microspheres have better actuation performances. Furthermore, the actuator with 1 μm PS microspheres has larger bending deformation compared to that with 0.6 μm PS microspheres.

Finally, the cycling stability of MXene actuators and MXene/PS-MXene actuators (1 μm PS microspheres) was compared at 1.5 V, 2 Hz square wave voltage as shown in Fig. 5(a). In the first 100 cycles, the peak-to-peak displacement of MXene actuators gradually increases with increasing cycle number, which might be due to the gradual opening of ion channels during repeated bending. Then the peak-to-peak displacement of MXene actuators reaches a stable state in subsequent cycles and finally reaches ca. 1.1 times of initial displacement. However, MXene/PS-MXene actuators have no process of increasing peak-to-peak displacement because the change of ion pathways allows ions to migrate smoothly in the electrode, making MXene/PS-MXene actuators reach the maximum displacement at the beginning. After 10,000 cycles, the peak-to-peak displacement can still maintain 90% of initial displacement. Both of MXene actuators and MXene/PS-MXene actuators have good cyclic stability and this might be attributed to the good interlayer adhesion between the electrodes and the intermediate electrolyte. It can be seen from Fig. S12 in the ESM that after the cycle test, the morphology of the electrolyte layer in actuators has changed while the sandwiched structure of actuators is still maintained well.

In Fig. 5(b), it can be found that the 3D-structure electrochemical actuator based on MXene/PS-MXene electrodes presents larger bending strain under relatively lower applied voltage at the same frequency. Table S3 in the ESM shows the mechanical properties and actuation performance of MXene-based actuators and other actuators in the literature. Although MXene/PS-MXene actuators have a lower Young's modulus than MXene actuators, it already has a considerable Young's modulus in comparison with the mechanical properties of other different types of actuators. In addition, the peak-to-peak strain of MXene/PS-MXene actuators is not only much larger than that of MXene actuators but also greater than that of most actuators reported in literature.

4 Conclusion

In order to achieve large bending deformation under low applied voltage and fast ion diffusion and accumulation, we developed MXene-based electrochemical actuators with $Ti_3C_2T_x$ and its composite materials as the electrodes. The unimpeded ion pathways in the 3D MXene/PS-MXene hybrid electrode enhance ion diffusion and fast injection. In addition, the conductive network provided by MXene facilitates rapid electron transfer in electrodes. The fast ion diffusion and rapid electron transfer result in excellent actuation performance. The prepared electrochemical actuator based on the MXene/PS-MXene

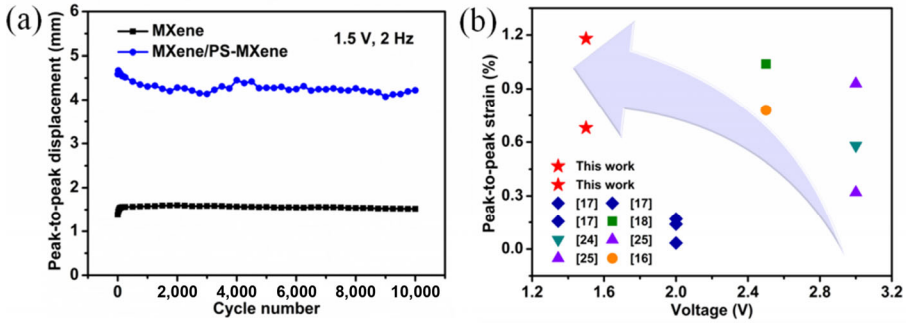

Figure 5 (a) Cyclic testing results of MXene actuators and MXene/PS-MXene actuators under a ± 1.5 V, 2 Hz square wave voltage. (b) The actuation performance of different electrochemical actuators under 0.1 Hz square wave voltage.

electrode exhibits excellent actuation performance with peak-to-peak strain of ca. 1.18%, good cyclic durability with 90% retention after 10,000 cycles and considerable mechanical properties with Young's modulus of ca. 246 MPa. Such high-performance actuators could be used in various fields such as artificial arms and bionic robots.

Acknowledgements

This work was supported by the National Key Basic Research Program of China (Grant No. 2018YFA0208403), the National Natural Science Foundation of China (Grant Nos. 51861165103, 11832010, 11890682, and 21721002), and the Strategic Priority Research Program of Chinese Academy of Sciences (Grant Nos. XDB36000000 and XDB30020100).

Electronic Supplementary Material: Supplementary material (Characterization of materials and actuators, mechanical properties of electrode layers and electrolyte layers, the equivalent circuit model of EIS measurements, photographs of bending deformations, actuation performance of actuators, EIS molding data, the performance comparison of different electrochemical actuators and the video of the actuation performance of the MXene/PS-MXene actuator under a 1.5 V, 0.1 Hz square wave voltage) is available in the online version of this article at https://doi.org/10.1007/s12274-020-3222-x.

References

[1] Zhou, J.; Mulle, M.; Zhang, Y. B.; Xu, X. Z.; Li, E. Q.; Han, F.; Thoroddsen, S. T.; Lubineau, G. High-ampacity conductive polymer microfibers as fast response wearable heaters and electromechanical actuators. *J. Mater. Chem. C* **2016**, *4*, 1238–1249.

[2] Gural'skiy, I. A.; Quintero, C. M.; Costa, J. S.; Demont, P.; Molnár, G.; Salmon, L.; Shepherd, H. J.; Bousseksou, A. Spin crossover composite materials for electrothermomechanical actuators. *J. Mater. Chem. C* **2014**, *2*, 2949–2955.

[3] Ze, Q. J.; Kuang, X.; Wu, S.; Wong, J.; Montgomery, S. M.; Zhang, R. D.; Kovitz, J. M.; Yang, F.; Qi, H. J.; Zhao, R. K. Magnetic shape memory polymers with integrated multifunctional shape manipulation. *Adv. Mater.* **2020**, *32*, 1906657.

[4] Diller, E.; Zhuang, J.; Lum, G. Z.; Edwards, M. R.; Sitti, M. Continuously distributed magnetization profile for millimeter-scale elastomeric undulatory swimming. *Appl. Phys. Lett.* **2014**, *104*, 174101.

[5] Priimagi, A.; Barrett, C. J.; Shishido, A. Recent twists in photoactuation and photoalignment control. *J. Mater. Chem. C* **2014**, *2*, 7155–7162.

[6] Yu, L.; Cheng, Z. X.; Dong, Z. J.; Zhang, Y. H.; Yu, H. F. Photomechanical response of polymer-dispersed liquid crystals/graphene oxide nanocomposites. *J. Mater. Chem. C* **2014**, *2*, 8501–8506.

[7] Hua, D. C.; Zhang, X. Q.; Ji, Z. Y.; Yan, C. Y.; Yu, B.; Li, Y. D.; Wang, X. L.; Zhou, F. 3D printing of shape changing composites for constructing flexible paper-based photothermal bilayer actuators. *J. Mater. Chem. C* **2018**, *6*, 2123–2131.

[8] Li, W. W.; Zhao, L. Y.; Dai, Z. H.; Jin, H.; Duan, F.; Liu, J. C.; Zeng, Z. H..; Zhao, J.; Zhang, Z. A temperature-activated nanocomposite metamaterial absorber with a wide tunability. *Nano Res.* **2018**, *11*, 3931–3942.

[9] Oh, J.; Kozlov, M. E.; Carretero-González, J.; Castillo-Martínez, E.; Baughman, R. H. Thermal actuation of graphene oxide nanoribbon mats. *Chem. Phys. Lett.* **2011**, *505*, 31–36.

[10] Maeda, S.; Hara, Y.; Sakai, T.; Yoshida, R.; Hashimoto, S. Self-walking gel. *Adv. Mater.* **2007**, *19*, 3480–3484.

[11] Behl, M.; Lendlein, A. Shape-memory polymers. *Mater. Today* **2007**, *10*, 20–28.

[12] Park, K.; Yoon, M. K.; Lee, S.; Choi, J.; Thubrikar, M. Effects of electrode degradation and solvent evaporation on the performance of ionic-polymer-metal composite sensors. *Smart Mater. Struct.* **2010**, *19*, 075002.

[13] Kong, L. R.; Chen, W. Carbon nanotube and graphene-based bioinspired electrochemical actuators. *Adv. Mater.* **2014**, *26*, 1025–1043.

[14] Li, J. Z.; Ma, W. J.; Song, L.; Niu, Z. Q.; Cai, L.; Zeng, Q. S.; Zhang, X. X.; Dong, H. B.; Zhao, D.; Zhou, W. et al. Superfast-response and ultrahigh-power-density electromechanical actuators based on hierarchal carbon nanotube electrodes and chitosan. *Nano Lett.* **2011**, *11*, 4636– 4641.

[15] Cottinet, P. J.; Souders, C.; Tsai, S. Y.; Liang, R.; Wang, B.; Zhang, C. Electromechanical actuation of buckypaper actuator: Material properties and performance relationships. *Phys. Lett. A* **2012**, *376*, 1132–1136.

[16] Lu, C.; Yang, Y.; Wang, J.; Fu, R. P.; Zhao, X. X.; Zhao, L.; Ming, Y.; Hu, Y.; Lin, H. Z.; Tao, X. M. et al. High-performance graphdiyne-based electrochemical actuators. *Nat. Commun.* **2018**, *9*, 752.

[17] Lu, L. H.; Liu, J. H.; Hu, Y.; Zhang, Y. W.; Randriamahazaka, H.; Chen, W. Highly stable air working bimorph actuator based on a graphene nanosheet/carbon nanotube hybrid electrode. *Adv. Mater.* **2012**, *24*, 4317–4321.

[18] Wu, G.; Wu, X. J.; Xu, Y. J.; Cheng, H. Y.; Meng, J. K.; Yu, Q.; Shi, X. Y.; Zhang, K.; Chen, W.; Chen, S. High-performance hierarchical black-phosphorous-based soft electrochemical actuators in bioinspired applications. *Adv. Mater.* **2019**, *31*, 1806492.

[19] Wu, G.; Li, G. H.; Lan, T.; Hu, Y.; Li, Q. W.; Zhang, T.; Chen, W. An interface nanostructured array guided high performance electrochemical actuator. *J. Mater. Chem. A* **2014**, *2*, 16836–16841.

[20] Lu, L. H.; Liu, J. H.; Hu, Y.; Zhang, Y. W.; Chen, W. Graphene-stabilized silver nanoparticle electrochemical electrode for actuator design. *Adv. Mater.* **2013**, *25*, 1270–1274.

[21] Terasawa, N.; Ono, N.; Hayakawa, Y.; Mukai, K.; Koga, T.; Higashi, N.; Asaka, K. Effect of hexafluoropropylene on the performance of poly(vinylidene fluoride) polymer actuators based on single-walled carbon nanotube-ionic liquid gel. *Sens. Actuators B Chem.* **2011**, *160*, 161–167.

[22] Terasawa, N.; Ono, N.; Mukai, K.; Koga, T.; Higashi, N.; Asaka, K. A multi-walled carbon nanotube/polymer actuator that surpasses the performance of a single-walled carbon nanotube/polymer actuator. *Carbon* **2012**, *50*, 311–320.

[23] Liu, Q.; Liu, L. Q.; Xie, K.; Meng, Y. N.; Wu, H. P.; Wang, G. R. ; Dai, Z. H.; Wei, Z. X.; Zhang, Z. Synergistic effect of a *r*-GO/PANI nanocomposite electrode based air working ionic actuator with a large actuation stroke and long-term durability. *J. Mater. Chem. A* **2015**, *3*, 8380–8388.

[24] Wu, G.; Hu, Y.; Zhao, J. J.; Lan, T.; Wang, D. X.; Liu, Y.; Chen, W. Ordered and active nanochannel electrode design for high-performance electrochemical actuator. *Small* **2016**, *12*, 4986–4992.

[25] Wu, G.; Hu, Y.; Liu, Y.; Zhao, J. J.; Chen, X. L.; Whoehling, V.; Plesse, C.; Nguyen, G. T. M.; Vidal, F.; Chen, W. Graphitic carbon nitride nanosheet electrode-based high-performance ionic actuator. *Nat. Commu.n* **2015**, *6*, 7258.

[26] Kotal, M.; Kim, J.; Kim, K. J.; Oh, I. K. Sulfur and nitrogen co-doped graphene electrodes for high-performance ionic artificial muscles. *Adv. Mater.* **2016**, *28*, 1610–1615.

[27] Roy, S.; Kim, J.; Kotal, M.; Tabassian, R.; Kim, K. J.; Oh, I. K. Collectively exhaustive electrodes based on covalent organic framework and antagonistic co-doping for electroactive ionic artificial muscles. *Adv. Funct. Mater.* **2019**, *29*, 1900161.

[28] Roy, S.; Kim, J.; Kotal, M.; Kim, K. J.; Oh, I. K. Electroionic antagonistic muscles based on nitrogen-doped carbons derived from poly (triazine-triptycene). *Adv. Sci.* **2017**, *4*, 1700410.

[29] Naguib, M.; Mochalin, V. N.; Barsoum, M. W.; Gogotsi, Y. 25th anniversary article: MXenes: A new family of two-dimensional materials. *Adv. Mater.* **2014**, *26*, 992–1005.

[30] Khazaei, M.; Ranjbar, A.; Arai, M.; Sasaki, T.; Yunoki, S. Electronic properties and applications of MXenes: A theoretical review. *J. Mater. Chem. C* **2017**, *5*, 2488–2503.

[31] Zang, X. N.; Chen, W. S.; Zou, X. L.; Hohman, J. N.; Yang, L. J.; Li, B. X.; Wei, M. S.; Zhu, C. H.; Liang, J. M.; Sanghadasa, M. et al. Self-assembly of large-area 2D polycrystalline transition metal carbides for hydrogen electrocatalysis. *Adv. Mater.* **2018**, *30*, 1805188.

[32] Ahmed, B.; Anjum, D. H.; Hedhili, M. N.; Gogotsi, Y.; Alshareef, H. N. H_2O_2 assisted room temperature oxidation of Ti_2C MXene for Li-ion battery anodes. *Nanoscale* **2016**, *8*, 7580–7587.

[33] Li, Z. X.; Ma, C.; Wen, Y. Y.; Wei, Z. T.; Xing, X. F.; Chu, J. M.; Yu, C. C.; Wang, K. L.; Wang, Z. K. Highly conductive dodecaborate/MXene composites for high performance supercapacitors. *Nano Res.* **2020**, *13*, 196–202.

[34] Boota, M.; Gogotsi, Y. MXene-conducting polymer asymmetric pseudocapacitors. *Adv. Energy Mater.* **2019**, *9*, 1802917.

[35] Song, X. L.; Wang, H.; Jin, S. M.; Lv, M.; Zhang, Y.; Kong, X. D.; Xu, H. M.; Ma, T.; Luo, X. Y.; Tan, H. F. et al. Oligolayered $Ti_3C_2T_x$ MXene towards high performance lithium/sodium storage. *Nano Res.* **2020**, *13*, 1659–1667.

[36] Lei, Y. J.; Zhao, W. L.; Zhang, Y. Z.; Jiang, Q.; He, J. H.; Baeumner, A. J.; Wolfbeis, O. S.; Wang, Z. L.; Salama, K. N.; Alshareef, H. N. A MXene-based wearable biosensor system for high-performance *in vitro* perspiration analysis. *Small* **2019**, *15*, 1901190.

[37] Li, T. K.; Chen, L. L.; Yang, X.; Chen, X.; Zhang, Z. H.; Zhao, T. T.; Li, X. F.; Zhang, J. H. A flexible pressure sensor based on an MXene-textile network structure. *J. Mater. Chem. C* **2019**, *7*, 1022–1027.

[38] Li, X. L.; Yin, X. W.; Han, M. K.; Song, C. Q.; Xu, H. L.; Hou, Z. X.; Zhang, L. T.; Cheng, L. F. Ti_3C_2 MXenes modified with *in situ* grown carbon nanotubes for enhanced electromagnetic wave absorption properties. *J. Mater. Chem. C* **2017**, *5*, 4068–4074.

[39] Li, X. L.; Yin, X. W.; Han, M. K.; Song, C. Q.; Sun, X. N.; Xu, H. L.; Cheng, L. F.; Zhang, L. T. A controllable heterogeneous structure and electromagnetic wave absorption properties of Ti_2CT_x MXene. *J. Mater. Chem. C* **2017**, *5*, 7621–7628.

[40] Bian, R. J.; He, G. L.; Zhi, W. Q.; Xiang, S. L.; Wang, T. W.; Cai, D. Y. Ultralight MXene-based aerogels with high electromagnetic interference shielding performance. *J. Mater. Chem. C* **2019**, *7*, 474–478.

[41] Yun, T.; Kim, H.; Iqbal, A.; Cho, Y. S.; Lee, G. S.; Kim, M. K.; Kim, S. J.; Kim, D.; Gogotsi, Y.; Kim, S. O. et al. Electromagnetic shielding of monolayer MXene assemblies. *Adv. Mater.* **2020**, *32*, 1906769.

[42] Pang, D.; Alhabeb, M.; Mu, X. P.; Dall'Agnese, Y.; Gogotsi, Y.; Gao, Y. Electrochemical actuators based on two-dimensional $Ti_3C_2T_x$ (MXene). *Nano Lett.* **2019**, *19*, 7443–7448.

[43] Umrao, S.; Tabassian, R.; Kim, J.; Nguyen, V. H.; Zhou, Q. T.; Nam, S.; Oh, I. K. MXene artificial muscles based on ionically cross-linked $Ti_3C_2T_x$ electrode for kinetic soft robotics. *Sci. Robot.* **2019**, *4*, eaaw7797.

[44] Ling, Z.; Ren, C. E.; Zhao, M. Q.; Yang, J.; Giammarco, J. M.; Qiu, J. S.; Barsoum, M. W.; Gogotsi, Y. Flexible and conductive MXene films and nanocomposites with high capacitance. *Proc. Natl. Acad. Sci. USA* **2014**, *111*, 16676–16681.

[45] Zhu, M. S.; Huang, Y.; Deng, Q. H.; Zhou, J.; Pei, Z. X.; Xue, Q.; Huang, Y.; Wang, Z. F.; Li, H. F.; Huang, Q. et al. Highly flexible, freestanding supercapacitor electrode with enhanced performance obtained by hybridizing polypyrrole chains with MXene. *Adv. Energy Mater.* **2016**, *6*, 1600969.

[46] Sun, R. H.; Zhang, H. B.; Liu, J.; Xie, X.; Yang, R.; Li, Y.; Hong, S.; Yu, Z. Z. Highly conductive transition metal carbide/carbonitride (MXene)@polystyrene nanocomposites fabricated by electrostatic assembly for highly efficient electromagnetic interference shielding. *Adv. Funct. Mater.* **2017**, *27*, 1702807.

[47] Alhabeb, M.; Maleski, K.; Anasori, B.; Lelyukh, P.; Clark, L.; Sin, S.; Gogotsi, Y. Guidelines for synthesis and processing of two-dimensional titanium carbide ($Ti_3C_2T_x$ MXene). *Chem. Mater.* **2017**, *29*, 7633–7644.

[48] Lukatskaya, M. R.; Bak, S. M.; Yu, X. Q.; Yang, X. Q.; Barsoum, M. W.; Gogotsi, Y. Probing the mechanism of high capacitance in 2D titanium carbide using *in situ* X-ray absorption spectroscopy. *Adv. Energy Mater.* **2015**, *5*, 1500589.